Detection of microwave emission due to rock fracture as a new tool for geophysics: A field test at a volcano in Miyake Island, Japan

Tadashi Takano, Takashi Maeda, Yoji Miki, Sayo Akatsuka, Katsumi Hattori, Masahide Nishihashi, Daishi Kaida, and Takuya Hirano

Tadashi Takano, College of Science and Technology, Nihon University, Funabashi, 274-8501, Japan. (takano@ecs.cst.nihon-u.ac.jp)

Takashi Maeda, Earth Observation Research Center (EORC), Japan Aerospace Exploration Agency (JAXA), Tsukuba, 305-8505, Japan. (maeda.takashi@jaxa.jp)

Yoji Miki, Ko-ei Co., Ltd., Yokohama, 223-8503, Japan.

Sayo Akatsuka, Atom Studio Co., Ltd., Tokyo, 160-0022, Japan.

Katsumi Hattori, Daishi Kaida, and Takuya Hirano, Graduate School of Science, Chiba University, Chiba, 263-8522, Japan.

Masahide Nishihashi, Meteorological Research Institute, Tsukuba, 305-0052, Japan

Abstract

This paper describes a field test to verify a newly discovered phenomenon of microwave emission due to rock fracture in a volcano. The field test was carried out on Miyake Island, 150 km south of Tokyo. The main objective of the test was to investigate the applicability of the phenomenon to the study of geophysics, volcanology, and seismology by extending observations of this phenomenological occurrence from the laboratory to the natural field.

We installed measuring systems for 300 MHz, 2 GHz, and 18 GHz- bands on the mountain top and mountain foot in order to discriminate local events from regional and global events. The systems include deliberate data subsystems that store slowly sampled data in the long term, and fast sampled data when triggered. We successfully obtained data from January to February 2008. During this period, characteristic microwave pulses were intermittently detected at 300 MHz. Two photographs taken before and after this period revealed that a considerably large-scale collapse occurred on the crater cliff. Moreover, seismograms obtained by nearby observatories strongly suggest that the crater subsidence occurred simultaneously with microwave signals on the same day during the observation period.

For confirmation of the microwave emission caused by rock fracture, these microwave signals must be clearly discriminated from noise, interferences, and other disturbances. We carefully discriminated the microwave data taken at the mountaintop and foot, checked the lightning strike data around the island, and consequently concluded that these microwave signals could not be attributed to lightning. Artificial interferences were discriminated by the nature of their waveforms. Thus, we inferred that the signals detected

36 at 300 MHz were due to rock fractures during cliff collapses. This result may provide a useful new tool for

37 geoscientists and for the mitigation of natural hazards.

38

1. Introduction

Japan has suffered several huge earthquakes in recent history. In particular, the Great East Japan Earthquake in March 2011 resulted in the death of about 20,000 people and caused heavy damage to houses and social infrastructure including the Fukushima nuclear power station (Cyranoski and Brumfiel, 2011). In light of such events, a greater demand than ever is placed on seismologists to clarify the mechanism of great earthquakes and to predict their occurrence (Sagiya, 2012).

These requirements are currently not realistic (Uyeda *et al.*, 2012). One reason may be the lack of knowledge and experience. In addition, study tools are limited to monitoring data from mechanical vibration sensors (Fujinawa and Noda, 2007) and remote sensing measurements of ground deformation (Massonnet *et al.*, 1993). Therefore, new tools are required, such as those in the field of electro-magnetic measurements, measurements of the Earth's atmosphere and ionosphere, and hydrological instruments. Among these approaches, however, the VAN method of ground potential measurement (Varotsos *et al.*, 1993) lacks an understandable explanation of the causes of the signals, and it is difficult to discriminate the signal from the noise. The correlation between the ionospheric disturbances and earthquakes needs a physical explanation, which could be provided by laboratory experiments (Molchanov and Hayakawa, 1998).

Meanwhile, microwave emission at 300 MHz, 2 GHz, and 22 GHz due to fracturing rock was recently found for the first time ever in laboratory experiments (Maki *et al.*, 2006). Generally, measurements of electromagnetic emissions at microwave bands are particularly difficult because the emitted signal's frequency is extremely high, and it has instantaneous properties with a considerably small time constant.

58 Maki *et al*. exploited a novel measuring system that includes an antenna and a low noise amplifier for each
59 of three frequency bands, and a large memory with excellent triggering. They used rock samples of quartzite,
60 granite, gabbro, and basalt for experiments. Electromagnetic emissions at 300 MHz and 2 GHz were detected
61 as for all rock samples though the emission at 22 GHz was detected only in the case of quartzite due to the
62 measurement difficulty. These emissions were not thermally excited and were discriminated from thermal
63 noises. At 300 MHz and 2 GHz, the received power was largest for quartzite and gabbro, the second largest
64 for granite, and the smallest for basalt. It is important that gabbro emits more power than granite though
65 gabbro includes less quartz than granite. Accordingly, this phenomenon is related to not only piezoelectricity
66 but also other rock properties such as stiffness and hardness, but has not yet been explained completely
67 (Takano *et al.*, 2010; Takano *et al.*, 2011). Therefore, the detection of microwave emission may offer a new
68 tool to geosciences and seismic geophysics.
69 Before the above-mentioned finding, Geng *et al.* (1999) reported microwave emission from rock fractures,
70 but could not confirm the waveform, spectrum, or power level. There have also been reports of
71 electromagnetic emissions at lower frequencies (Cress *et al.*, 1987; Nitsan *et al.*, 1977). In addition, it is
72 known that volcanic plumes are electrically charged because of the ejection of ions and atoms, vaporization
73 of water, and wind effects, and that the electromagnetic energy in volcanic plumes can be emitted at lower
74 frequencies (James *et al.*, 2008). A proposed mechanism for the electromagnetic emissions at lower
75 frequencies is the polarization effect due to piezoelectricity and charge movement when piezoelectric rocks
76 fracture. However, this model cannot explain the strong emission from gabbro, which has been confirmed

77 experimentally (Maki *et al.*, 2006). A model of current flow along the surface due to electrical charging was
78 proposed, based on friction and crack generation during fracture (O'Keefe *et al.*, 1995). However, the time
79 constant in this case is about 130 μs, so the high frequency cannot be explained with polarization due to
80 piezoelectricity or the movement of charges, which were adopted in Yoshida and Ogawa (2004). A model
81 that includes discharge across a microcrack could explain the experimental results of the waveforms (Maki
82 and Takano, 2004). Charge arising from bond dislocation between atoms or thermally excited electrons may
83 cause relatively high voltages in some materials (Ohnishi *et al.*, 2007). Kinetic excitation of the inner
84 electrons and the nucleus, rather than the outermost electrons, could explain the experimental emission
85 power results and the weak dependency on piezoelectricity (Takano *et al.*, 2010).
86 It is certainly true that rock fracture occurs in association with volcanic activity and earthquakes (Takano
87 and Maeda, 2009). However, microwave detection during such natural events has not yet been reported or
88 described, probably because geoscientists did not know about the phenomenon and the relevant microwave
89 technology. Therefore, it is important to verify the validity in a field test, so that geoscientists can utilize the
90 newly found phenomenon as a study tool.
91 To investigate the validity of this technique, we planned a field test to detect possible emissions (Takano *et*
92 *al.*, 2008; Takano *et al.*, 2009). The objectives were: (1) to confirm microwave emission during naturally
93 occurring phenomena to support the experimental findings, (2) to confirm a method for extrapolating
94 experimental findings to large-scale events, and eventually (3) to show the applicability of the phenomenon
95 to geophysics studies.

96 We considered several types of rock fracture for the field test and compared the advantages and
97 disadvantages of each, as follows:
98 (1) Cliff collapse around the crater in a volcano: A suitable volcano can be selected according to its activity
99 history. The emitted microwave propagates through the air, so we can eliminate the ambiguity arising from
100 heterogeneity of attenuation during underground propagation.
101 (2) Volcanic eruption: A suitable volcano can be selected, but the interval between events may be too long,
102 and it may not be possible to predict the event well in advance. In addition, the expelled lava and hot rocks
103 may emit microwave noise due to thermal excitation, which is difficult to discriminate from emission due to
104 rock fracture.
105 (3) Earthquake: The location and time of the event cannot be predicted. Although attenuation has been well
106 studied recently (Hosono *et al.*, 2009), we still do not have sufficient knowledge of microwave attenuation
107 during underground propagation.
108 Therefore, at present, microwave signals due to rock fracture can be detected from cliff collapses more easily
109 than the other cases because of the known location and time, and can be considered an example of the
110 canonical problem (Yasukawa *et al.*, 2009). We thus decided to focus on the microwave signals emitted
111 during cliff collapses around the crater of a volcano.
112 This paper first describes the outline of the field test, including scientific as well as operational factors of
113 the test site. Then, the construction and characteristics of the measuring system are presented. The measuring
114 system was designed to support the acquisition of field data with limited funding and work force resources.

115 The correlation between detected microwave signals and changes in the cliff shape are described. Moreover,
116 the seismogram signals from nearby observatories are also compared to show further evidence that cliff
117 collapses occur at the same time as the microwave emissions. To demonstrate the reliability of the results, the
118 method for discriminating microwave signals from obstructive disturbances will be presented. The extent
119 and depth of analysis of other data types will be restricted only to aspects that relate to microwave emission
120 phenomena.

121 **2. Outline of the Test and Estimation of the Received Power**

122 In selecting the field test site, the following factors were considered: extent of volcanic activity, electric
123 power and communication infrastructure, seismometer network, transportation to the site, and the
124 researchers' security and accommodation. Comparing these factors among active volcanoes in Japan, we
125 selected Mount Oyama volcano on Miyake Island, which is located 150 km south of Tokyo, as shown in
126 Figure 1 (a). This volcano has been active since a large eruption in 2000, which forced all inhabitants of the
127 island to evacuate. Several volcanological and seismological studies have been performed on this large
128 eruption, and are helpful to our later data analysis (Ukawa *et al.*, 2000; Fujita *et al.*, 2001; Geshi *et al.*,
129 2002).

130 As shown in Figure 1 (b), the Japan Meteorological Agency (JMA) has installed six seismometers (MYCR,
131 MKJA, MIG2, MYSA, MYKO, and MYYA) around Miyake Island. These seismometers, in particular,
132 MYCR and MKJA, which are located around the crater, are useful for investigating tremors to determine
133 their hypocenter locations and to clarify their relation to the detected microwaves. The raw data from these

seismometers are not available to the public, but we obtained them through the cooperation of JMA.

Figure 2 shows an overview of our test sites at the top and foot of the mountain. Figure 2 (a) shows the positions of our test sites relative to the crater. The crater is about 1 km in diameter and 550 m in depth. We installed measuring systems at two observation sites at the top and foot of the mountain, denoted by square symbols. The two seismometers around the crater (MYCR and MKJA) are shown by black circles.

Figure 2 (b) shows the scenery around the test site at the top of the mountain. The antennas receive microwaves, which may be emitted by rock fracture around the crater cliff. The measuring instruments are located in an extreme environment very close to the crater, from which toxic gases including H_2S and SO_2 are emitted almost constantly. Furthermore, rain mixes with these gases to form a strong acid.

As shown in Figure 2 (b), at the test site at the top of the mountain, microwave antennas were pointed toward the crater cliff. The antennas' field of view (FOV) covered the crater cliff, as indicated by dotted lines in Figure 2 (a). Meanwhile, the microwave antennas at the test site at the mountain foot were pointed toward the zenith to receive microwave signals that cover the whole island.

Figure 3 shows the configuration of the entire measuring system. The observation frequencies are 300 MHz, 2 GHz, and 18 GHz. The first two frequencies are adopted in laboratory experiments on rock fractures (Maki *et al.*, 2006), and 18 GHz is the same frequency as that observed by the microwave radiometer AMSR-E on the remote sensing satellite Aqua (Kawanishi *et al.*, 2003). The use of high frequencies has several advantages over the use of lower frequencies, which include ease of calibration of the signal power, reduction of interference from a directional antenna, and an inherent low-noise environment. Observations

were carried out from November 2007 until May 2009 with several interruptions resulting from measuring system failures.

Prior to the test, we calculated the relationship between received power and emitted power based on the test site parameters and the antenna gain. The microwave signal power emitted in association with rock fractures was calculated from extrapolation of the experimental data from the size of small laboratory sample to that of an actual fractured rock in the field. It was assumed that the crater cliff at which the rock fractured was at a distance of 2 km from the field antennas at most and that the volume of fractured rock was 4.2×10^3 m^3. The values of the emitted power in the laboratory experiment were calculated using the waveforms from quartzite reported in Maki *et al.* (2006), because this is the only study that successfully measured all frequencies of 300 MHz, 2 GHz, and 22 GHz. The comparison between frequencies and the power estimation in optimal conditions can be accomplished using these values, though Miyake Island is composed predominantly of basalt. The received power was estimated as listed in Table 1.

For the noise characteristics of the receiving system, we were able to estimate the S/N ratio of the signal power according to the thermal noise power, as summarized in Table 1. The S/N ratio at 300 MHz is 31, which is large enough to allow the signal to be discriminated from the noise. The observation is marginal at 2 GHz, with an S/N ratio of 1.7, and may be impossible at 22 GHz, where the S/N ratio is less than unity.

3. Measuring System Constitution

The measuring system should be versatile enough to discriminate local phenomena relevant to crater cliff collapses on the mountain top from island-wide phenomena, as well as to simultaneously support regular

observations and detailed data analyses. As shown in the block diagram of Figure 3, the microwave receiving systems at the top of the mountain consist of a frequency-peculiar antenna and a microwave receiver (Rx) including a low noise amplifier for each of three frequency bands, a data storage device (HDD), and a data transmission link including HUB, Router, and Wi-Fi circuit. Each receiving system at the three different frequency bands is limited to narrow bandwidths that are called sub-bands. Gathering data from all sub-bands, we can obtain the spectrum information of the whole band from 300 MHz to 18 GHz. This configuration is inevitable due to the difficulty in using an ultra-wide band receiver including antenna. Electric power was supplied through cables from the mountain foot.

A similar receiving system was installed at the mountain foot, with the antennas pointing toward the zenith. In this configuration, the side lobe is at 90° relative to the main lobe, which points toward the target crater cliff. Therefore, the directivity at the angle to the cliff is -13.5 dB lower than at the main lobe, and the free-space loss from the collapsed cliff to the mountain foot antenna is 4.3 dB larger than that to the mountain top antenna, considering the distances in Figure 2(a). The received power at the foot site calculated from these two factors is -17.8 dB, which is 0.016 times weaker than that at the top site. This value is sufficiently small for the foot antenna to discriminate the real signals generated in rock fractures in the crater from the island-wide interference noise that could be detected by both antennas.

The detected signals were first sampled at a lower sampling rate of 1 kHz to reduce the frequency bandwidth, which enabled regular transmission to laboratories in Tokyo. Using this configuration, we monitored the operational status of the measuring system and obtained rough data within the limits imposed

191 by our communication capabilities. The circuit for detecting the received microwaves operates mostly in the
192 peak hold mode. In this mode, the peak value of a pulse is held for a time window of 1 ms. This mode is
193 equivalent to low-pass filtering to reduce the information rate. When a strong signal of a significant event is
194 detected, the data are sampled at a faster rate of 1 MHz. The strong signal is a trigger to activate faster
195 sampling. During faster sampling, the detection circuit operates in the rectified mode, which supplies the
196 absolute amplitude of observed microwave signals in frequency bands lower than 1 MHz. This mode is used
197 to evaluate the waveform precisely. The data saved during the faster sampling are transmitted occasionally
198 on a communication line or recorded to a hard disk. Note that the sampling rate is much lower than a radio
199 frequency or the intermediate frequency of a heterodyne receiver due to the limitation of the memory and
200 communication capabilities. This scheme, called an under-sampling system, gives the smallest limit of the
201 waveform.

202 For visual data, we initially used data from a video camera installed on the crater cliff; however, the
203 resolution was too poor to allow changes in the cliff to be recognized, and the camera accidentally fell to the
204 crater bottom. Photos taken on the occasions of our visit also provided valuable visual data, but the temporal
205 resolution was very limited.

206 **4. Results of Microwave Detection**

207 Many microwave signals were detected at 300 MHz during the test term from January 9 to February 4,
208 2008. In contrast, the 2-GHz signals were much weaker and were often contaminated with interference
209 signals, probably from a radar-transmitting antenna, and no 18.7-GHz signals were detected at all.

Figure 4 shows the time-series data for the 300-MHz signals detected in the slow sampling mode at the mountain top during the test period. In this figure, the data were examined every 10 s, and the largest amplitude in each time bin was plotted. Obvious interference signals were eliminated beforehand as described in the last paragraph of Section 6. Figure 4 indicates that the signals did not appear continuously, but rather intermittently in clusters. In particular, the signals detected on January 12 and on January 18 are the most significant but are quite different to one another in nature, having the greatest number of signals and the strongest signal, respectively. The reason for this difference will be clarified later using several auxiliary data types.

The data in Figure 4 were then processed to obtain the distribution according to the pulse amplitude, which is a basic statistical characteristic of the detected signals. The pulse amplitude indicates the initial peak of a decaying signal in the slow sampling mode. The receiving amplifier output includes not only signal power but also noise power, so we have to discriminate the true signal from the noise. Considering the noise level of our receiver, we set the discrimination level of a signal to be 0.08 V. Figure 5 shows the result. The number of pulses decreases exponentially up to a height of 1.35 V. Almost all pulses stronger than 1.35 V occurred on January 12 and 18. The percentage of pulses stronger than 1.35 V was 0.3 % of the total pulses.

The duration of a pulse varies significantly between detected signals. We defined the duration time of a pulse as the time lapse between the signal rising above and falling below the discrimination level of 0.08 V. Under this definition, a pulse can include more than one data sample in the duration time. We then analyzed the relationship between the duration and the pulse height. The result is shown in Figure 6. The black circle

229 for each pulse height represents the mean value of the durations. The lower and upper ends of the bar around
230 the black circle represent the minimum and maximum values of the durations. In this figure, three distinctive
231 groups of data can be observed.

232 The first group of pulses in Figure 6, indicated by P, extends through the abscissa range from 0 V to 3 V
233 with almost linear increases in duration. This trend is attributed to the time response of the receiver in the
234 peak hold mode, which is later explained using a concrete waveform shown in Figure 8 (b). Accordingly, the
235 duration depends on the peak amplitude. Usually, each data point in this trend is a single pulse, but two
236 pulses are included in the level from 2.35 V to 2.4 V, as shown in Figure 5. The strongest signal has a 3-V
237 pulse height and 50-ms duration and was detected on January 18. This group looks quite different from noise,
238 and is believed to include pulses generated by large cliff collapses over a short duration, as will be explained
239 later.

240 The second group is in the abscissa range from 0 V to 1.25 V with durations longer than 50 ms, and is
241 indicated by Q. There are more pulses at the lower pulse height, as shown in the distribution of Figure 5.
242 Therefore, this group corresponds to noise. Each datum in this group has maximum and minimum duration
243 values in addition to the mean value. The distribution of the duration inside each datum has a strongly biased
244 shape. For example, from 0.15 V to 0.2 V on the abscissa, the maximum value is 210 ms, but the mean value
245 is near 0 ms. This indicates that the although most pulses have short durations, a few pulses at this level have
246 notably long durations.

247 The third group of pulses is from 1.3 V to 1.45 V, from 1.6 V to 1.65 V, and from 2.15 V to 2.2 V on the

248 abscissa and is indicated by R. This group is extraordinarily high and wide, and the all pulses were detected
249 on January 12. It will be demonstrated later in this document that these signals were generated by lightning.
250 For confirmation of the origin of the signals, we extended the signal on January 12, which is shown in
251 Figure 4, and checked its relation with the signal obtained at the mountain foot site. The result for this day is
252 shown in Figure 7. In this figure, the orange and purple lines represent the signals at the mountaintop and
253 foot, respectively. The signals at the mountaintop are quite dense, with only small intervals between the two
254 time periods, while those at the mountain foot are sparser but occasionally have amplitudes comparable with
255 those at the mountain top.
256 We then extended the signal on January 18 in Figure 4, and show the change on that day with orange lines
257 in Figure 8. We can see quite a distinct difference in the signals on January 18 and that on January 12,
258 shown in Figure 7. In Figure 8 (a), the 300-MHz signals detected on January 18 consist of completely
259 separate events. At around 19:00, the strongest signal A was recorded, with an amplitude of 3 V at the
260 mountain top. This corresponds to the black circle indicated by A in Figure 5. Close to signal A, several
261 signals can be recognized, one of which is 1.6 V. At around 20:30, the strong signal B of 1.2 V was detected
262 with an associated signal of 1.0 V, and signal C was detected at around 22:00. In addition, there were two
263 weaker signals at around 05:00 and 14:00. Purple lines are added to the plots to represent the signals at the
264 mountain foot. For example, at the same time as signal A, a weak signal was also recorded. As the amplitude
265 of this signal is one-twentieth of the amplitude of signal A, and the decaying waveform is confirmed to be
266 similar to signal A, it is inferred that this signal was emitted at the crater cliff, and detected at the mountain

267 foot by the antenna side lobe. Signals B and C are also associated with much weaker signals. Accordingly,
268 signals A, B, and C are thought to have originated at the mountaintop.
269 After finding the impulse signals in Figure 8 (a), we can enlarge the waveform even more. Figure 8 (b)
270 shows signal B with an abscissa scale of 50 ms/ division. We can see the details of the signal, which is
271 composed of several pulses. The strongest pulse B1 lasts about 30 ms from 20:23:38.910. There is no signal
272 at the time of B1 at the mountain foot. Since the signal detector was operated in the peak hold mode, the
273 amplitude decays with a half-amplitude time constant, about 10 ms in this case. Therefore, we cannot
274 discriminate smaller pulses that are enclosed within this decaying envelope.
275 We can expand the waveforms in Figure 8 (b) even more using the fast sampling mode, as shown in Figure
276 9. In this mode, the detector output a rectified waveform from the microwave of both polarities. The
277 amplitude in Figure 9 is slightly different from that in Figure 8 (b) because they were not precisely calibrated.
278 From examining Figure 9, it becomes apparent that each pulse in Figure 8 (b) is actually composed of
279 thousands of short pulses.

280 **5. Correlation with Crater Cliff Collapses and Quakes**

281 A possible correlation between microwave emission and cliff collapse is studied in this section. We
282 photographed the shape of the crater cliff from a fixed observation point in a fixed magnification with the
283 same camera each time we visited the test site. Figs. 10 (a) and (b) show the cliff shapes on January 9, 2008
284 and November 11, 2008, respectively. Comparison of the two scenes indicates that areas 1, 2, and 3,
285 highlighted with red circles, all collapsed significantly.

In addition, we obtained an aerial photo taken by the Japan Coast Guard on March 11, 2008, shown in Figure 10 (c). In this figure, a white square symbol represents our test site at the mountaintop, and the red circles correspond to areas 1, 2, and 3 in Figure 10 (a). Based on Figure 10 (a) and Figure 10 (c), the time of the large collapse can be narrowed down to the period between January 9 and March 11, 2008.

To estimate the collapsed volume, we calculated the lateral size of the largest collapsed area, area 2, in Figure 10 (a) based on the view angles and the distances to the cliff. The normal thickness of area 2 was calculated from Figure 10 (c) comparing the dent with the crater diameter. Accordingly, the collapsed volume was modestly estimated to be 94,000 m^3, which is believed to be large enough to exceed the critical value for signal detection, as shown in Table 1. In addition, since other areas of the cliff including areas 1 and 3 collapsed, microwave signals were likely to be emitted several times.

To determine the time of cliff collapses more precisely, we can obtain and analyze seismological data from several observatories shown in Figure 2 (a). We first give an overview of the seismic signals from station MYCR, at the mountaintop. Figure 11 (a) shows the variation in the absolute ground velocity on January 18. The time scale is determined to be equal to Figures 7 and 8 (a) for comparison purposes. We can see many quake signals during the analyzed term because the station is located on an active volcano. The peaks, represented by diamonds, were classified as earthquakes or volcanic tremors by JMA, according to their amplitude, duration, and waveform. The peaks, represented by small black circles, were not recognized as earthquakes or volcanic tremors by the criteria of JMA. Accordingly, quakes due to cliff collapses may be included in the latter category. Figure 11 (b) shows the data from 18:00 to 22:00 in expanded form. The 300

MHz microwave signals A, B, and C in Figure 6 are included in Figure 11 (b). They coincide with increases in the absolute ground velocity (A', B', and C'). However, there are ambiguities in determining the timing because the time bin of microwave reception is 10 sec, which is comparable to the duration of the quake, and because of asynchronous measurement between the microwave receivers and the seismometer.

In contrast, a number of strong peaks of the seismogram at MYCR were not associated with corresponding microwave signals in Figure 11 (a), such as D' and E'. Naturally, not all of these peaks were generated by cliff collapses, because the seismograms also reflect earthquakes or volcanic tremors. The emitted microwave signals may not reach the receiving antenna, either because of the collapse location or because of the main lobe direction of the receiving antenna and radio wave being blocked by obstacles. Therefore, we will focus on particular times when analyzing the seismograms, especially around the time that microwave signals A, B, and C occurred, in order to extract common features of the seismograms in these events.

For comparison purposes, variations in the absolute ground velocity at MYCR and MKJA (mountain foot) on January 12 are shown in Figure 12. The symbols and lines are drawn similar to those in Figure 11, and gray lines and circles are added as MKJA data. At 11:00, a largest peak signal was detected, and it was three times larger than the largest signal on Jan 18. In fact, it rained heavily with lightning on this day. After a lightning strike at 12:18, the MYCR data were lost due to failure. In correspondence to this time, the microwave emission in Figure 7 is so dense that quakes happened at times that correspondent with microwave emissions. However, we cannot infer the physical relation between the microwave emission and seismogram due to the ambiguity of timing determination as described before.

According to previous studies (Ukawa *et al.*, 2000; Fujita *et al.*, 2001), seismograms associated with the volcanic activity in Miyake Island can be classified into the three types, as shown below:

(1) Volcano-tectonic event: The P and S waves can be clearly distinguished, as in a typical earthquake.

(2) Low-frequency (LF) earthquake: The P and S waves cannot be clearly distinguished. The dominant frequency in the waveform is lower than 1 Hz. The waveform slowly rises, lasts more than several tens of seconds, and slowly decays. LF earthquakes are likely to indicate magma migration.

(3) Swarm-like activity of LF earthquakes: These events have features similar to those of type (2) events, but the dominant frequency in the waveform is higher than that of type (2) events. This event was observed a few hours before tilt steps and originated at shallow depths (0–2 km) around a crater.

Fujita *et al.* (2001) suggested that type (3) is associated with crater subsidence, which is actually similar to a cliff collapse. In addition, these seismogram features were studied in cases of landslides and glacier collapses, and presented in Dammeier *et al.* (2011) and Feng (2011). Therefore, let us view the details of the waveforms in some instances in reference to the above-mentioned classification.

The seismograms at MYCR, MKJA, MYKO, MIG2, MYSA, and MYYA for quake A' in Figure 11 are shown in Figure 13. In these seismograms, the origins of the abscissa axes are the same (18:44:57). For all components (NS, EW, and UD), MYCR, located on the mountaintop, was excited first and had the strongest amplitudes. Then a few seconds later, MKJA at the mountain foot was excited. In contrast, MYKO, MIG2, MYYA, and MYSA at the coastal area were much more weakly excited with a greater delay. Accordingly, the hypocenter of quake A' was located closer to MYCR than other seismometers. If the hypocenter were

343 deep underground, the distances to all observatories would be almost equal each other. Therefore, it is
344 reasonable to conclude that the hypocenter is located close to the ground surface. In addition, the dominant
345 frequency in the waveform at MYCR is higher than 1 Hz, which coincides with the features of type (3)
346 events. Accordingly, quake A' is inferred to be generated by a cliff collapse.

347 Next, all seismograms for quake B' are shown in Figure 14. The origins of the abscissa axes are the same
348 (20:20:28). For all components, MYCR was excited first and had the strongest amplitudes. A few seconds
349 later, MKJA was excited. MIG2 and MYSA, located in the coastal area, were excited another several seconds
350 later. MYKO and MYYA at the coastal area were quite weakly excited. Accordingly, the hypocenter of quake
351 B' was located nearest to MYCR and close to the ground surface. The waveform at MYCR coincides with
352 the features of type (3) events. Accordingly, quake B' is also inferred to be generated by a cliff collapse.

353 The seismograms for quake C' are shown in Figure 15. Only MYCR showed the features of type (3) events,
354 while the other seismograms barely showed any peaks. Therefore, quake C' is also inferred to be generated
355 by a cliff collapse. Consequently, we conclude that the seismograms for A', B', and C' indicate the cliff
356 collapses that simultaneously generated microwave emissions A, B, and C, as shown in Figure 11 (b).
357 However, these conclusions have ambiguity, as several other seismograms also show the same features as A',
358 B', and C'.

359 In contrast, all the seismograms for event D' shown in Figure 11 (a) are shown in Figure 16. The origins of
360 the abscissa axes are the same (00:25:42). The P and S waves can be clearly distinguished for all components
361 as is a feature of type (1) events. In addition, the amplitudes measured by MYCR, MKJA, MIG2, and MYYA

were excited almost simultaneously and with similar amplitude, though MYCR was the most strongly excited among all seismometers. Therefore, the distances from the hypocenter of quake D' to MYCR, MKJA, MIG2, and MYYA were almost the same, and thus the hypocenter was not located near the crater surface. Accordingly, around the time of D', no cliff collapse occurred, and this agrees with the fact that no 300-MHz microwave signals were detected, as indicated in Figure 8 (a).

A strong seismometer signal was also detected at E', as shown In Figure 11 (a). The relevant seismogram from MYCR is shown in Figure 17. Only the up-down component changed significantly, in the down direction, while the north-south and east-west components were completely quiet. Therefore, we regard this response as an instrumental error.

6. Discrimination from Obstructing Factors

Several factors obstruct the detection of microwave signals generated from rock fractures. The first factor is emission due to lightning. Lightning is caused by movement of electrical charge in the air. The temporal change of this movement is represented by a rectangular pulse with a width T and height A. Its frequency spectrum is then $(A/\pi f)$ sin (πfT), where f is its frequency, which would extend through the 300 MHz band. However, the nature of lightning at microwave frequencies has not been reported so far. Considering the high sensitivity of our receiver, we cannot rule out the influence of lightning on our receiver at 300 MHz. Accordingly, we thoroughly investigated the occurrence of lightning during the eight periods listed in Table 2 when strong 300 MHz microwave signals were detected on the mountain top, as shown in Figure 4.

Lightning strike data were provided by the Japan Lightning Detection Network (JLDN) (Ishii *et al.*, 2005),

which determines the locations of lightning strikes using sensors installed throughout Japan. The lightning sensors observe the LEMP (lightning electromagnetic impulse) in frequency ranges from VLF (3–30 kHz) to LF (30–300 kHz). The lightning sensor closest to the test site is on Kouzu Island, 30 km northwest of Miyake Island.

According to JLDN, the only lightning strike detected near the crater in the periods shown in Table 2 was at 12:18 on January 12, 2008. Figure 7 indicates that the two microwave signals at 12:18 were the strongest on this day, and that several signals were received simultaneously at the mountaintop and foot. The meteorological data also reported that it rained heavily with lightning most of the time, and that it did not rain in the periods from 0:00 to 3:00 and from 21:00 to 24:00 on this day. This raining time clearly corresponds to the period of microwave emission in Figure 7. Accordingly, many signals were likely to be caused by lightning. Group R in Figure 6 is typical of data that originates from lightning. Note that the other data in Figure 6 might have originated from lightning but cannot be discriminated from data that originated from the other sources. On the other hand, the weather was completely clear with no lightning observed on January 18, according to the meteorological data.

The second factor is rain, which has a strong correlation with lightning. Rain changes the electrical characteristics of the ground. Therefore, we gathered meteorological data on the precipitation in the periods shown in Table 2. It rained only on January 12, 2008, while the weather was clear without rain on the other days.

The third factor is artificial radio interference. Two kinds of artificial interference were observed in several

400 cases, as shown in Figure 18. One of them has a regular periodicity in the waveform, and the other has an
401 abrupt appearance with a high frequency component and an offset of the noise level. The interference signals
402 were differentiate by finding the waveforms and by comparison of signal levels at the mountaintop and the
403 mountain foot. We succeeded in eliminating this interference through filtering.

404 **7. Conclusions**

405 A field test was carried out in the extreme environment of the volcano at Miyake Island. The novel
406 measuring system worked well but with several interruptions. Microwave signals were detected
407 intermittently at 300 MHz. Each signal was composed of pulses with quite narrow widths, which were
408 estimated to be several μs from the fast-sampling data. We performed a statistical analysis of the received
409 signals to identify peculiarities in several cases. There were extraordinarily high-amplitude pulses in the
410 slow-sampling data on two days: January 12, 2008 and January 18, 2008.

411 It was revealed by photos of the rock cliff that the volcanic crater significantly changed in shape between
412 January 9 and March 11, 2008. Analysis of seismograms indicated subsidence of the crater rather than
413 typical earthquakes. Local quake activity at shallow depths was verified by the seismograms installed around
414 the island. The correlation between the microwave emissions and ground quakes was significant. These facts
415 strongly support the case that separate microwave pulses on January 18, 2008 were generated by cliff
416 collapses.

417 By using meteorological data and comparing the detection data collected at the mountaintop with that
418 collected at the mountain foot, we concluded that the dense group of pulses on January 12, 2008 originated

419 from lightning. Meanwhile, several artificial interferences were observed, but we differentiated and
420 eliminated them with our filtering software.

421 Overall, microwave emission was detected during volcanic activity and is believed to be generated by rock
422 fracture in cliff collapses. Microwave emission associated with rock fracture is a newly discovered
423 phenomenon, and we can conceive many applications for it in scientific and practical fields. This technique
424 may offer a new scientific tool for geophysics and rock physics research. It is already known that microwave
425 emission is closely related to microcrack occurrence and the resultant voltage generation (Maki *et al.*, 2004).
426 Therefore, the relationship of material parameters such as brittleness, hardness, and electric conductivity
427 with microwave emission should be clarified. In addition, the domain structure of a material could be
428 investigated using microwave diagnosis.

429 In practical applications, the results described in this paper offer the possibility that this technique could be
430 applied to volcano monitoring. The same technique could also be applied to other natural disasters associated
431 with rock fractures, such as earthquakes and landslides. Indeed, we have already developed a data analysis
432 method for extracting local and faint microwave anomalies from the data obtained from a satellite-borne
433 microwave sensor, and have successfully detected the signature of a volcanic eruption and an earthquake
434 (Maeda and Takano, 2008; Maeda and Takano, 2010). However, the timescale of the hazardous event and the
435 relevant rock fracture has not yet been clarified. If rock fractures around an asperity before a great
436 earthquake, this technique could be valuable for mitigating social losses by predicting earthquake
437 occurrence.

438 **Acknowledgments.** We thank the Japan Meteorological Agency and Dr. S. Yoshida and Dr. K. Nagata of the
439 Earthquake Research Institute, University of Tokyo, for arranging the observation site, providing
440 seismometer data, and discussing the obtained results. We express our gratitude to the Japan Coast Guard for
441 providing photographs of the cliff collapse. Finally, we thank Dr. K. Tachikawa of JAXA for his continuous
442 support for this project.

443 **References**

444 Cress, G. O., B. T. Brady, and G. A. Rowell (1987), Sources of electromagnetic radiation from fracture of
445 rock samples in the laboratory, *Geophys. Res. Lett., 14,* 331 – 334.

446 Cyranoski, D. and G. Brumfiel (2011), Fukushima impact is still hazy: Chaos and bureaucracy hamper
447 assessment of nuclear crisis, *Nature, 477,* 139-140.

448 Dammeier, F., Moore, J., Haslinger, F., & Loew, S. (2011), Characterization of alpine rockslides using
449 statistical analysis of seismic signals, *Journal of Geophysical Research, 116, F04024,* DOI: 10.1029
450 /2011JF002037.

451 Feng, Z. (2011), The seismic signatures of the 2009 Shiaolin landslide in Taiwan, Natural Hazards and Earth
452 *System Science, 11,* 1559-1569 DOI: 10.5194/nhess-11-1559-2011

453 Fujinawa, Y. and Y. Noda (2007), Research and development of earthquake early warning-application
454 systems for various users, *BUTSURI-TANSA, 60, 5,* 375-386.

455 Fujita, E., M. Ukawa, E. Yamamoto, Y. Okada, and M. Kikuchi (2001), Volcanic Earthquakes and Tremors
456 Associated with the 2000 Miyakejima Volcano Eruption (in Japanese), *J. of Geography, 110(2),* 191-203.

457 Geng, N., M. Deng and C. Cui (1999), Simulated experimental studies on earthquake prediction by using
458 infrared and microwave remote sensing, Atmospheric and Ionospheric Electromagnetic Phenomena
459 Associated with Earthquakes, ed. by M. Hayakawa, *Terra Scientific Publishing Company (TERRAPUB),*
460 *Tokyo,* 751 – 758.
461 Geshi, N., T. Shimano, T. Chiba and S. Nakada (2002), Caldera collapse during the 2000 eruption of
462 Miyakejima Volcano, Japan, *Bull. Volcanol., 64,* 55 - 68.
463 Hosono, K., H. Osada, K. Saegusa and T. Takano (2009), Microwave propagation loss in a ground crack
464 larger than a wavelength, *Proc. the 2008 IEICE General Conference,* B-2-3.
465 Ishii, M., M. Saito, F. Fujii, J. Hojo, M. Matsui, N. Itamoto and K. Shinjo (2005), LEMP from Lightning
466 Discharges Observed by JLDN, *IEEJ Trans. on Power and Energy, 125, 8,* 765 – 770.
467 James, M. R., Wilson, L., Lane, S. J., Gilbert, J. S., Mather, T. A., Harrison, R. G., and Martin, R. S. (2008),
468 Electrical Charging of Volcanic Plumes, *Space Science Reviews, 137, 1-4,* 399-418, doi:10.1007/s11214-008-
469 9362-z.
470 Kawanishi, T., T. Sezai, Y. Ito, K. Imaoka, T. Takeshima, Y. Ishido, A. Shibata, M. Miura, H. Inahata and R.
471 W. Spencer (2003), The advanced microwave scanning radiometer for the earth observing system (AMSR-E),
472 NASDA's contribution to the EOS for global energy and water cycle studies, *IEEE Trans. on Geoscience and*
473 *Remote Sensing, 41, 2,* 184 – 194.
474 Massonnet, D., M. Rossi, C. Carmona, F. Adragna, G. Peltzer, K. Feigl and T. Rabaute (1993), The
475 displacement field of the Landers earthquake mapped by radar interferometry, *Nature, 364,* 138-142.

476 Maeda, T. and T. Takano (2008), Discrimination of Local and Faint Changes from Satellite-borne Microwave
477 Radiometer Data, *IEEE Trans. on Geoscience and Remote Sensing, 46, 9,* 2684 – 2691.
478 Maeda, T. and T. Takano (2010), Detection Algorithm of Earthquake-related Rock Failures from
479 Satelliteborne Microwave Radiometer Data, *IEEE Trans. on Geoscience and Remote Sensing, 48, 4,* 1768 –
480 1776.
481 Maki, K. and Takano, T. (2004), Analysis of the microwave radiation field from the discharge due to an
482 impact destruction (in Japanese), *National Convention of the Institute of Electrical Engineers of Japan*
483 *(IEEJ),* 1-081, 87.
484 Maki K., T. Takano, E. Soma, K. Ishii, S. Yoshida and M. Nakatani (2006), An experimental study of
485 microwave emission from compression failure of rocks, *J. of the Seismological Society of Japan, 58, 4,* 375 –
486 384.
487 Molchanov, O., and Hayakawa, M. (1998), Subionospheric VLF signal perturbations possibly related to
488 earthquakes, *J. Geophys. Res., 103, 17,* 489-504.
489 Nitsan, U. (1977), Electromagnetic emission accompanying fracture of quartz-bearing rocks, *Geophys. Res.*
490 *Lett., 4,* 333 – 336.
491 Ohnishi, H., Chiba, S., Soma, E., Ishii, K., Maki, K., Takano, T., and Hasegawa, S. (2007), Study on
492 microwave emission mechanisms on the basis of hypervelocity impact experiments on various targat plates,
493 *J. Appl. Phys., 101, 9,* 124901-1-8.
494 O'Keefe, S. G., and D. V. Thiel (1995), A mechanism for the production of electromagnetic radiation during

495 fracture of brittle materials, *Phys. Earth Planet. Inter., 89,* 127 – 135.

496 Sagiya, T. (2012), Suggestions for the future of seismology from the temporary committee (summary), *Japan*

497 *Geoscience Union Meeting 2012,* U06-01.

498 Takano T. *et al.* (2008), Detection of Microwave Frequency Signals from Earthquakes and Volcanic

499 Activities, *AGU Fall Meeting 2008,* S13C-1837.

500 Takano T. *et al.* (2009), Signal Detection of Microwave Frequency due to Rock Fracture in Volcanic

501 Activities, *Geophysical Research Abstracts, 11,* EGU2009-9176.

502 Takano T. and T. Maeda (2009), Experiment and Theoretical Study of Earthquake Detection Capability by

503 Means of Microwave Passive Sensors on a Satellite, *IEEE Geosci and Remote Sensing Lett., 6, 1,* 107 – 111.

504 Takano, T., H., Ikeda, and T. Maeda (2010), Consideration of the Mechanism of Microwave Emission Due to

505 Material Destruction, *J. Appl. Phys., 108,* 083722, 1-5.

506 Takano T., H. Ikeda, S. Sugita and T. Maeda, (2010), Consideration on the Mechanism of Microwave

507 Emission Due to Rock Fracture, *Geophysical Research Abstracts, 12,* EGU2010-6398.

508 Takano T., K. Maki, E. Soma, K. Hattori and T. Maeda (2011), Fundamentals of Microwave Detection in

509 Association with Rock Fracture and Experimental Data for Various Rocks, *Geophysical Research Abstracts,*

510 *13,* EGU2011-9638.

511 Ukawa, M., E. Fujita, E. Yamamoto, Y. Okada, and M. Kikuchi (2000), The 2000 Miyakejima eruption:

512 Crustal deformation and earthquakes observed by the NIED Miyakejima observation network, *Earth Planets*

513 *Space, 52(8),* xix–xxvi.

514 Uyeda, S. *et al.* (2012), Proposal for Earthquake Prediction Program I: Short-term Prediction, *Japan*
515 *Geoscience Union Meeting 2012,* U06-03.
516 Varotsos, P., Alexopoulos, K and Lazaridou, M. (1993), Latest aspects of earthquakes prediction in Greece
517 based on seismic electric signals, *Two, Tectonophysics, 224,* 1-37.
518 Yasukawa, H., I. Takumi, and M. Hata (2009), Signal detection technology on earth diastrophism using
519 electromagnetic wave observation, *International Symposium on Intelligent Signal Processing and*
520 *Communication Systems 2009,* 473 - 476.
521 Yoshida, S. and T. Ogawa (2004), Electromagnetic emissions from dry and wet granite associated with
522 acoustic emissions, *J. Geophys. Res., 109,* B09204, doi 10.1029/2004JB003092.

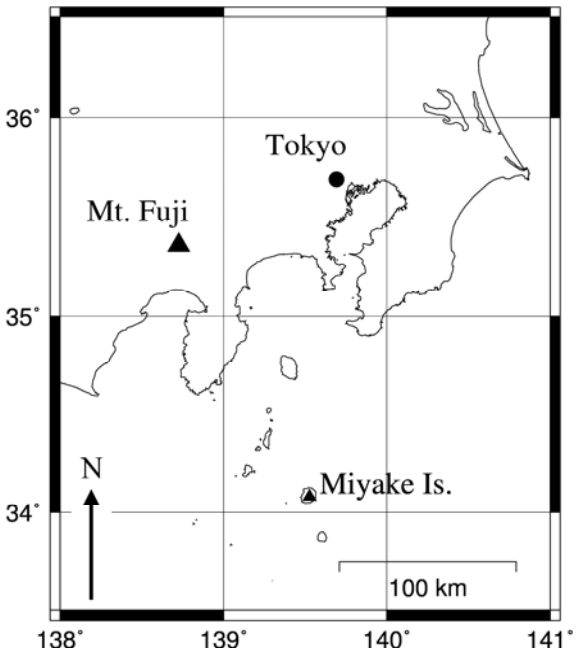

(a) Location of Miyake Island.

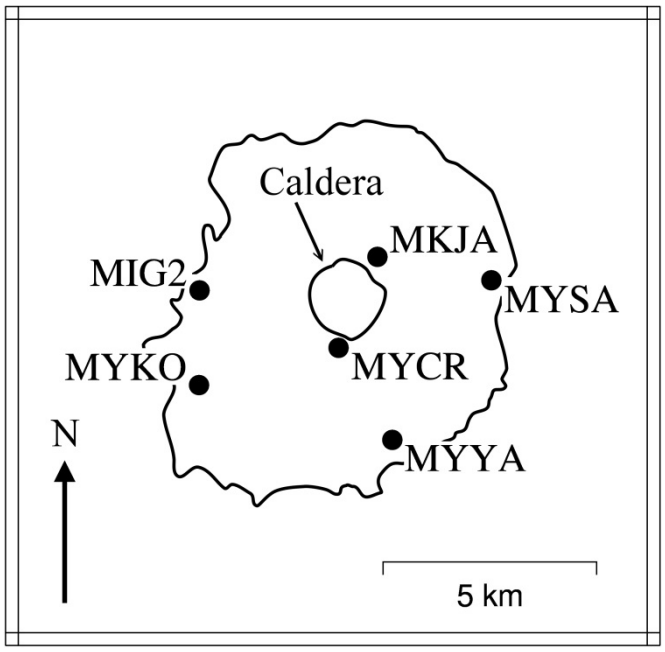

(b) Seismometer network in Miyake Island.

Figure 1. Overview of Miyake Island.

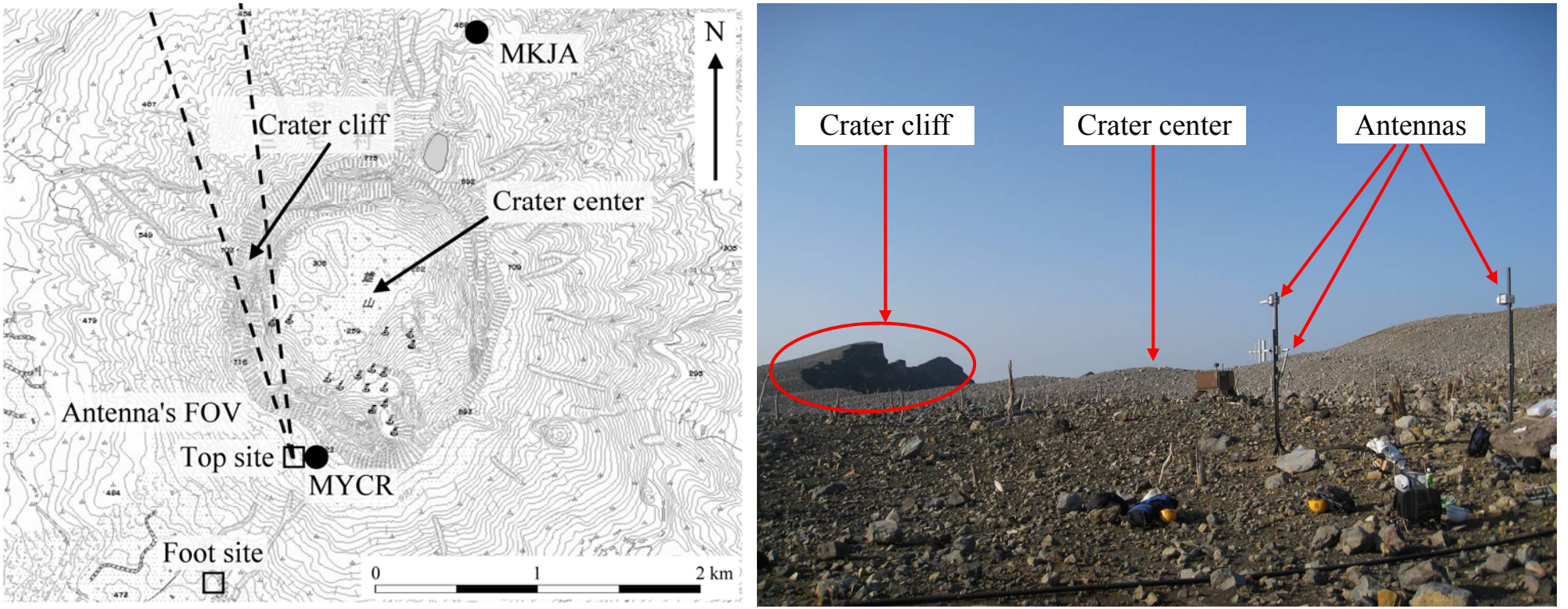

(a) Locations of our test sites at the top and foot of the mountain.

(b) Scenery around the test site at the mountaintop.

Figure 2. Overview of our test sites at the top and foot of the mountain at Miyake Island.

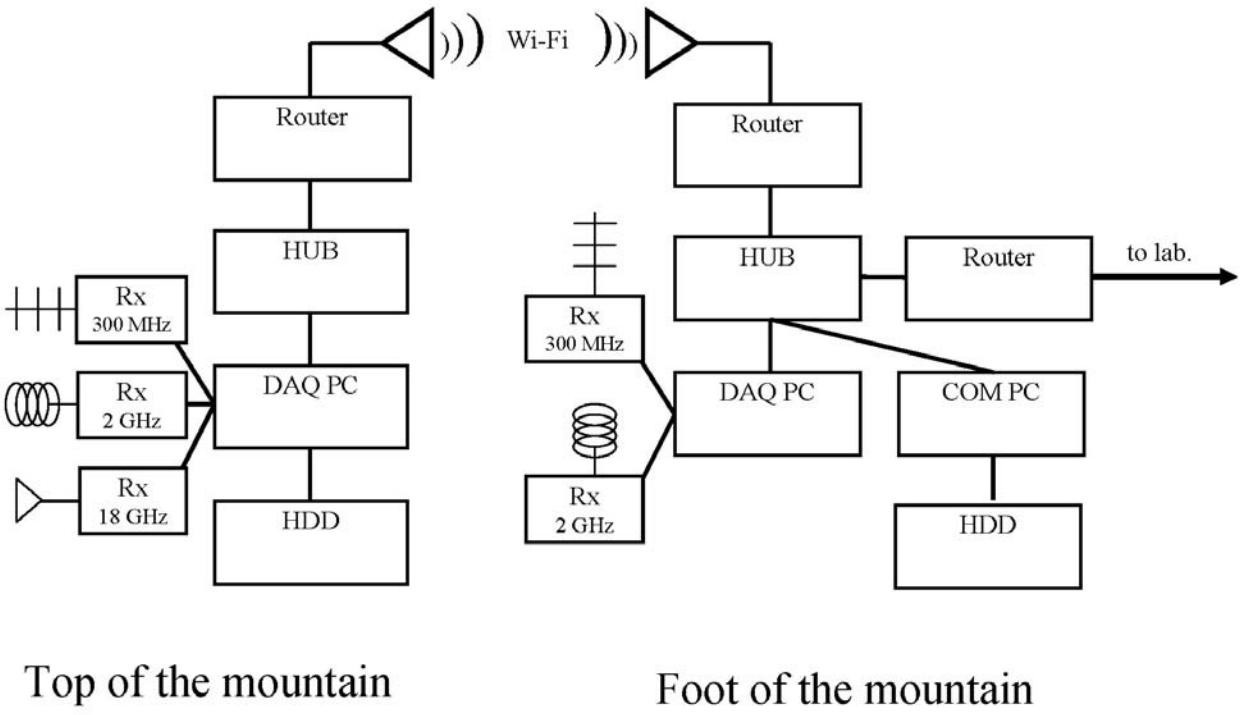

Figure 3. Configuration of the total measuring system. Rx: Receiver, DAQ PC: Data Acquisition PC, HDD: Hard Disk Drive, COM PC: Communication PC.

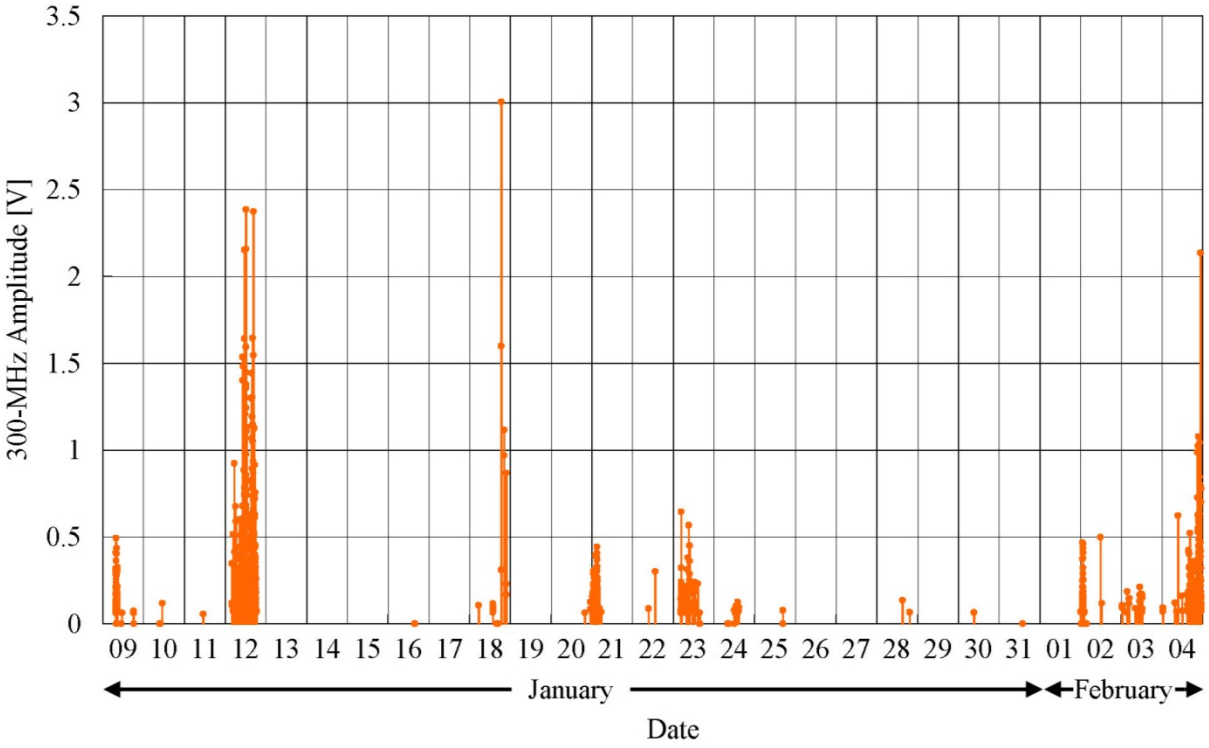

Figure 4. Accumulated 300-MHz signals at the top of the mountain during the test term f) to February 4, 2008.

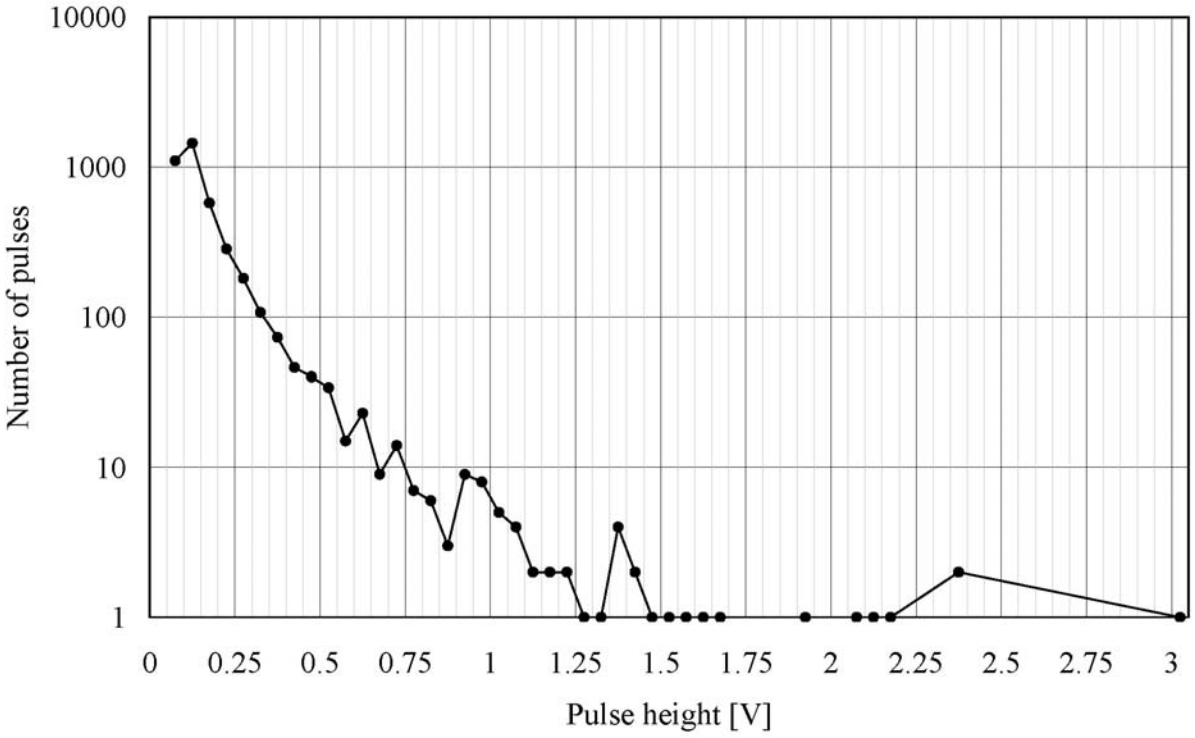

Figure 5. Relationship between the number of pulses and the pulse height for all signals detected at 300 MHz.

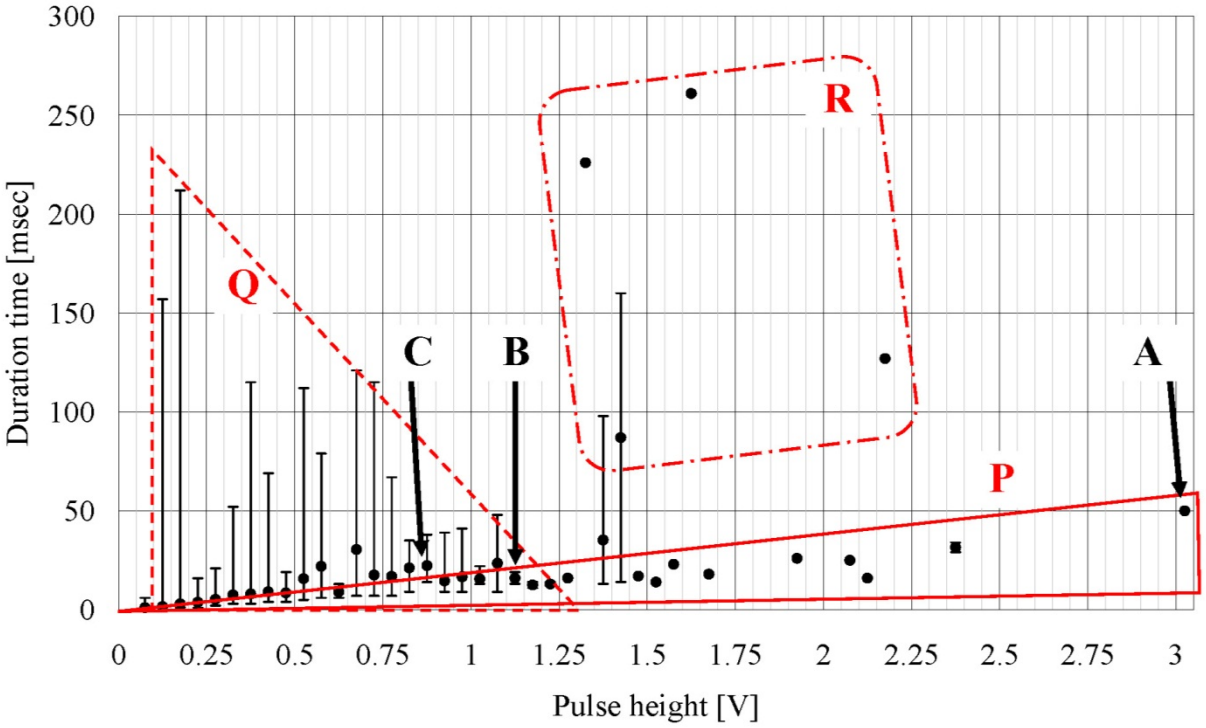

Figure 6. Relationship between the duration and the pulse height for all signals detected at 300 MHz. The black circle for each pulse height represents the mean value of the durations. The lower and upper ends of the bar around the black circle represent the minimum and maximum values of the durations.

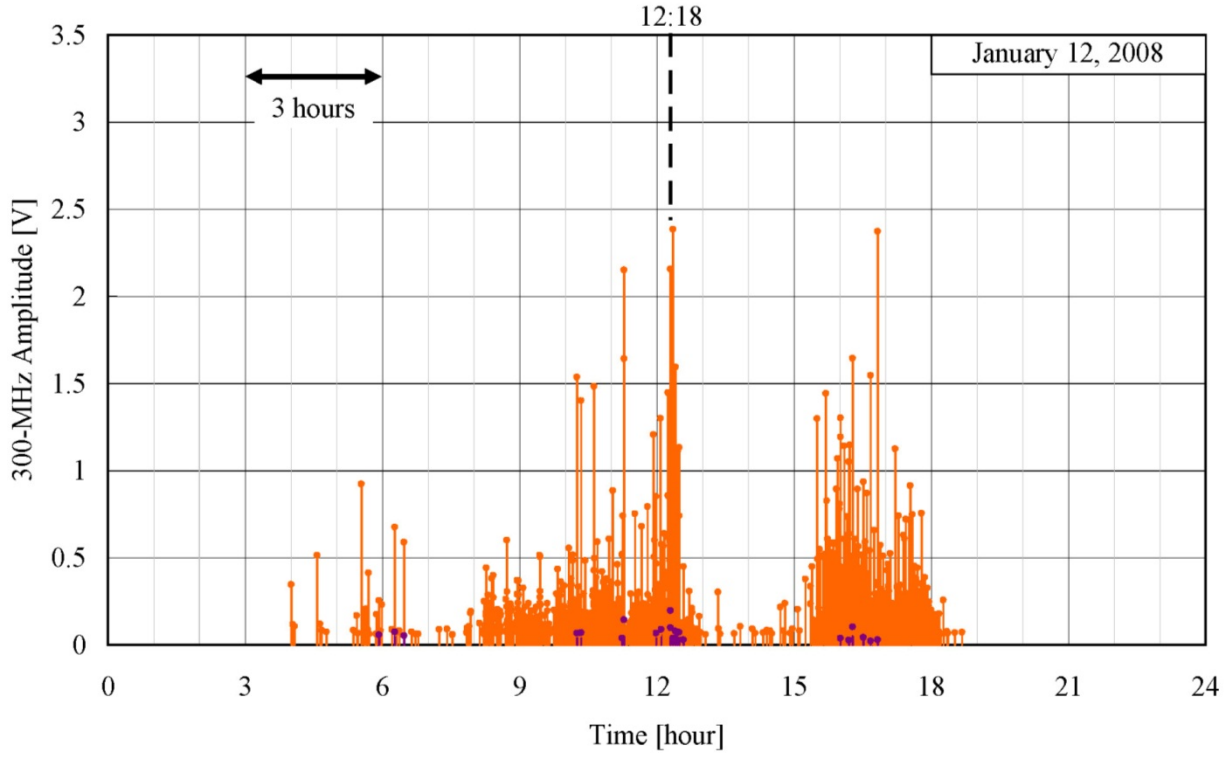

Figure 7. 300-MHz signals detected in the slow sampling mode on January 12. The orange (purple) line represents the 300-MHz signals at the top (foot) of the mountain. Both signals were strongest at 12:18 on this day.

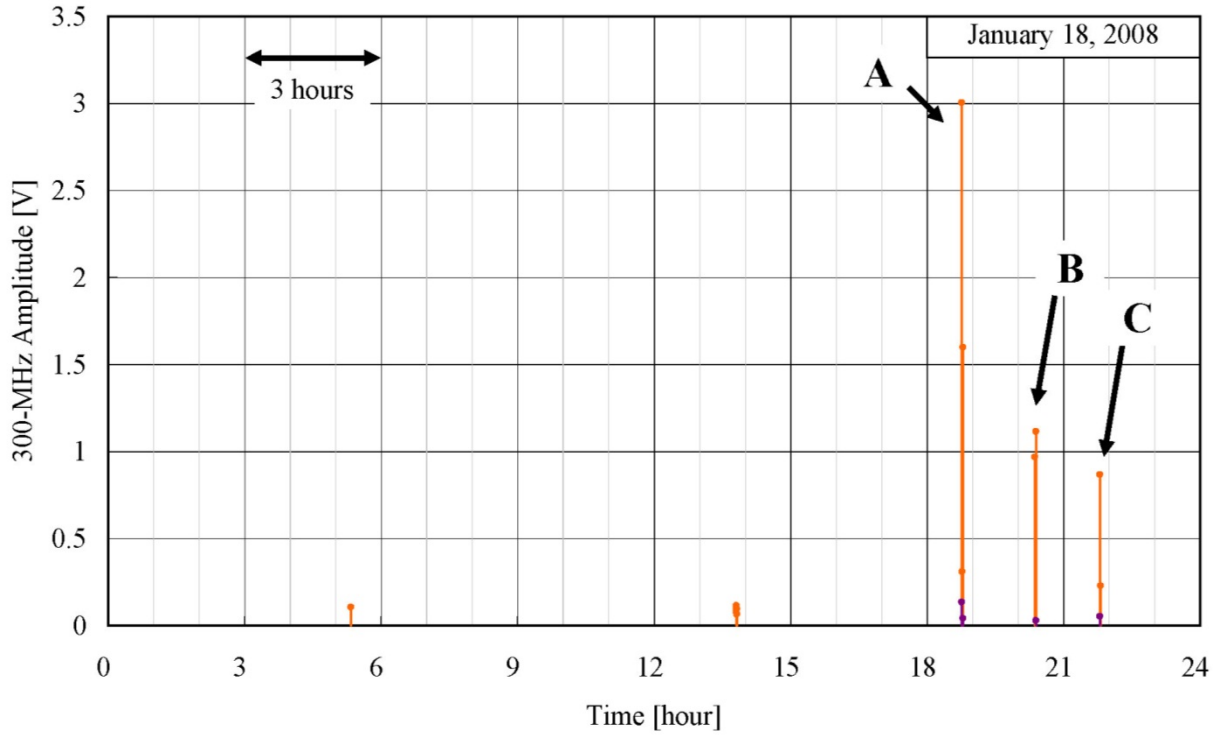

(a) Diurnal changes of detected signals. There are three groups of pulses (A, B, and C).

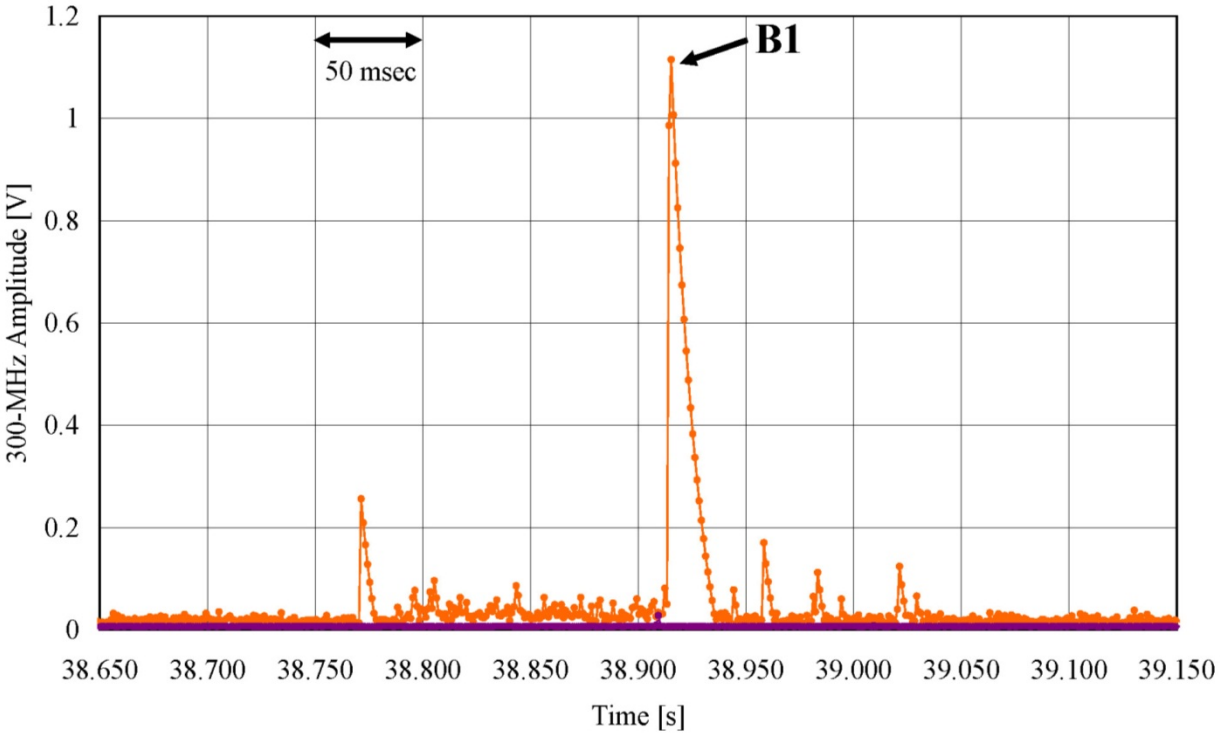

(b) Waveforms in signal B from 20:23:38.650 to 20:23:39.150.

Figure 8. 300-MHz signals detected in the slow sampling mode on January 18, 2008. In each figure, the orange (purple) line represents 300-MHz signals at the top (foot) of the mountain.

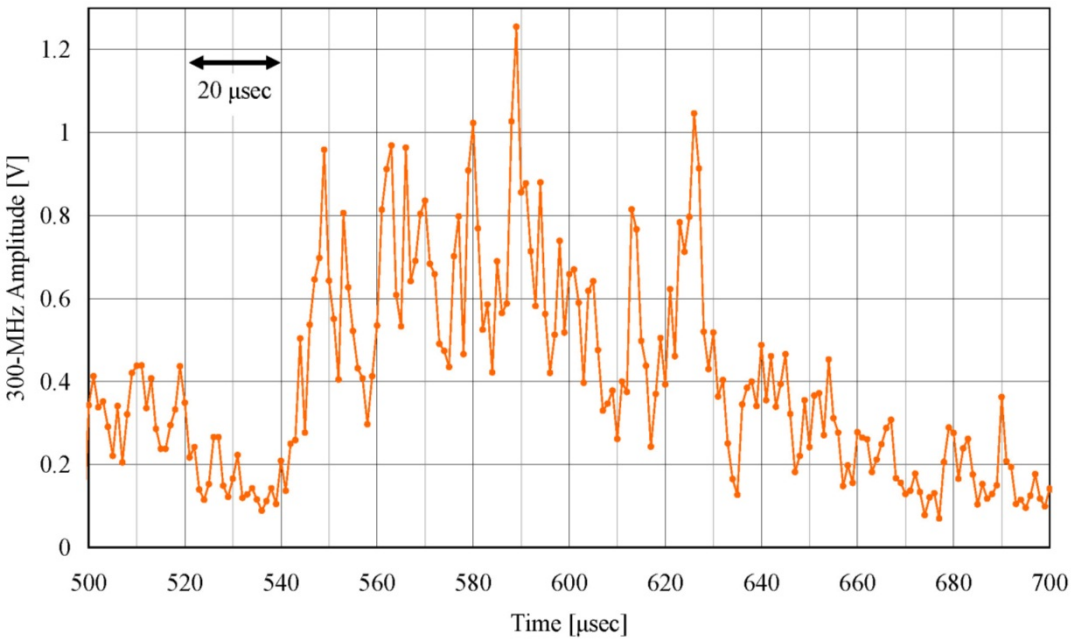

Figure 9. Expanded waveform of the impulse signal B1 in the fast sampling mode at 20:23:38.910.

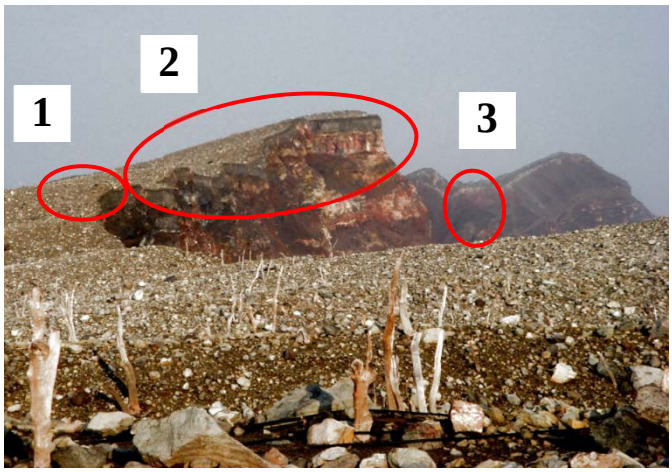

(a) Photo taken from the top site on January 9, 2008

(b) Photo taken from the top site on November 11, 2008

(c) Aerial photo taken on March 11, 2008 (courtesy of Japan Coast Guard). A red circle indicates a crater cliff with the large collapse.

Figure 10. Change of the shape of the crater cliff.

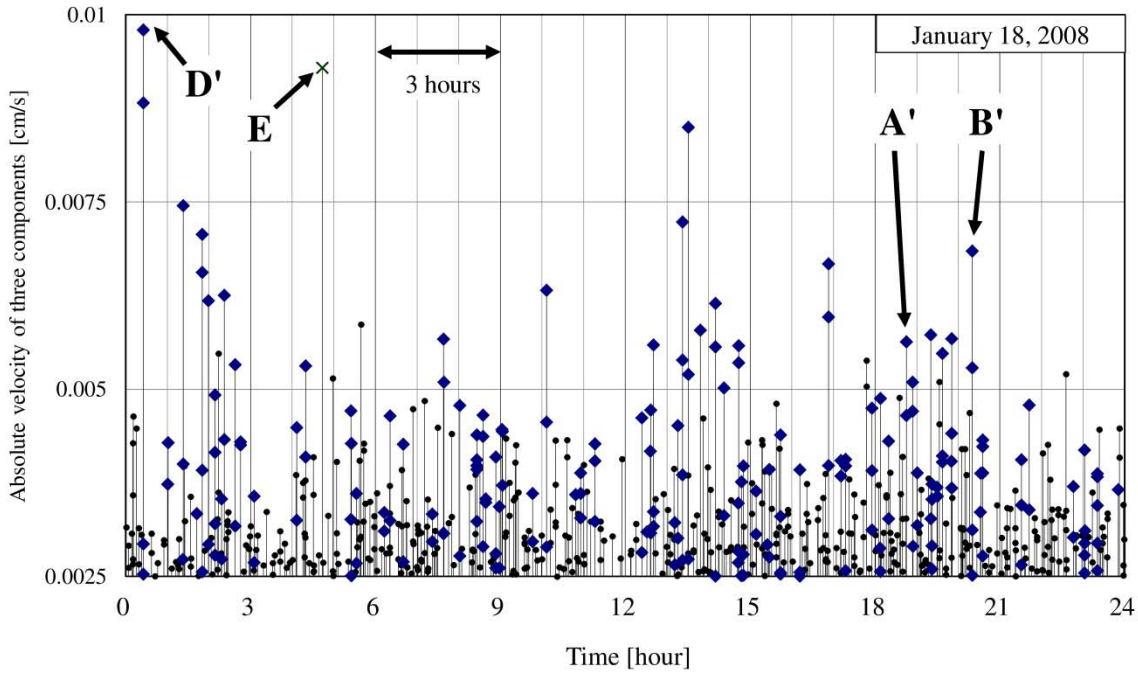

(a) Diurnal change

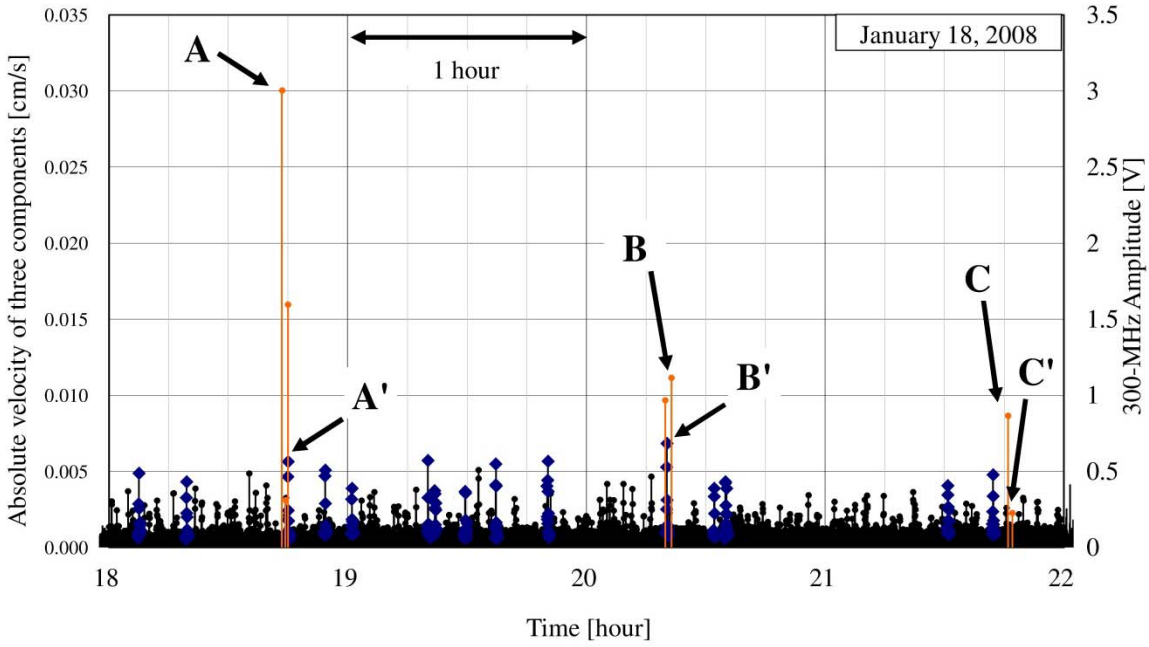

(b) Detailed temporal change with microwave signals

Figure 11. Variation in the absolute ground velocity at MYCR (mountaintop) on January 18. The peaks represented by diamonds were classified as earthquakes or volcanic tremors according to their amplitude, duration, and waveform by JMA. A, B, and C in the lower panel indicate the microwave signals shown in Figure 8 (a). A', B' and C' indicate the absolute ground velocity coincident with the microwave signals A, B and C. The D' and E' indicate examples not accompanied by microwave signals. In particular, the E' expressed by X symbol is considered as an errot in data (See Figure 16).

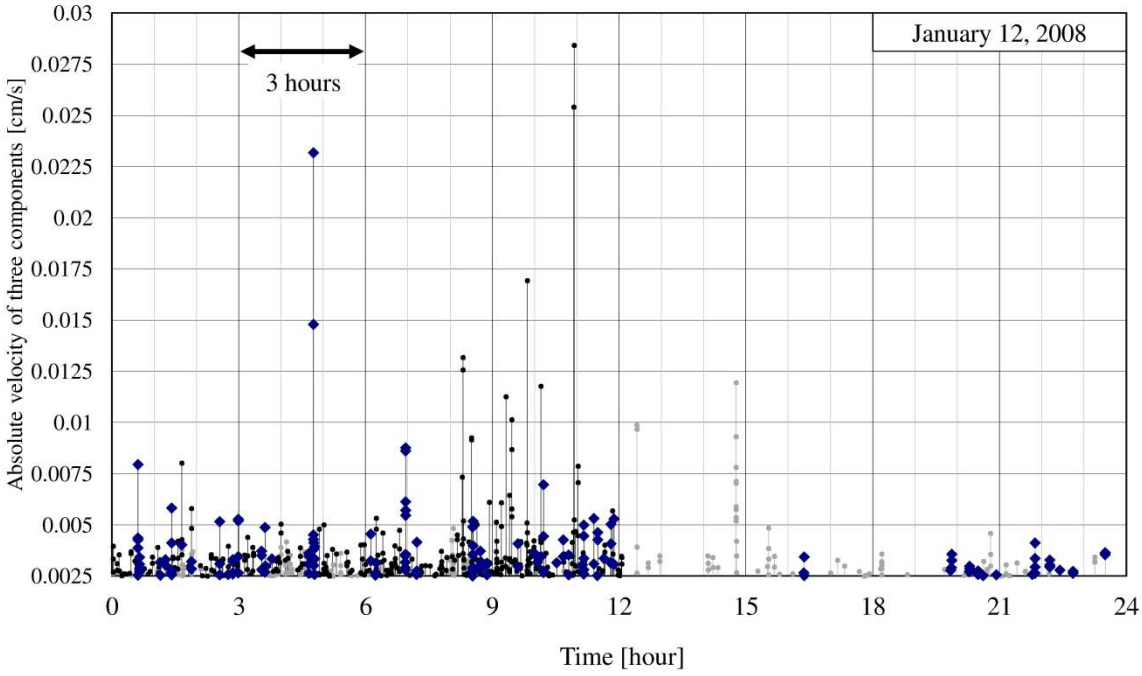

Figure 12. Variations in the absolute ground velocity at MYCR (mountaintop) and MKJA (mountain foot) on January 12. The symbols and lines are drawn similarly to Figures 11, and gray lines and circles are added as for MKJA data.After 12:18, the MYCR data were lost due to failure.

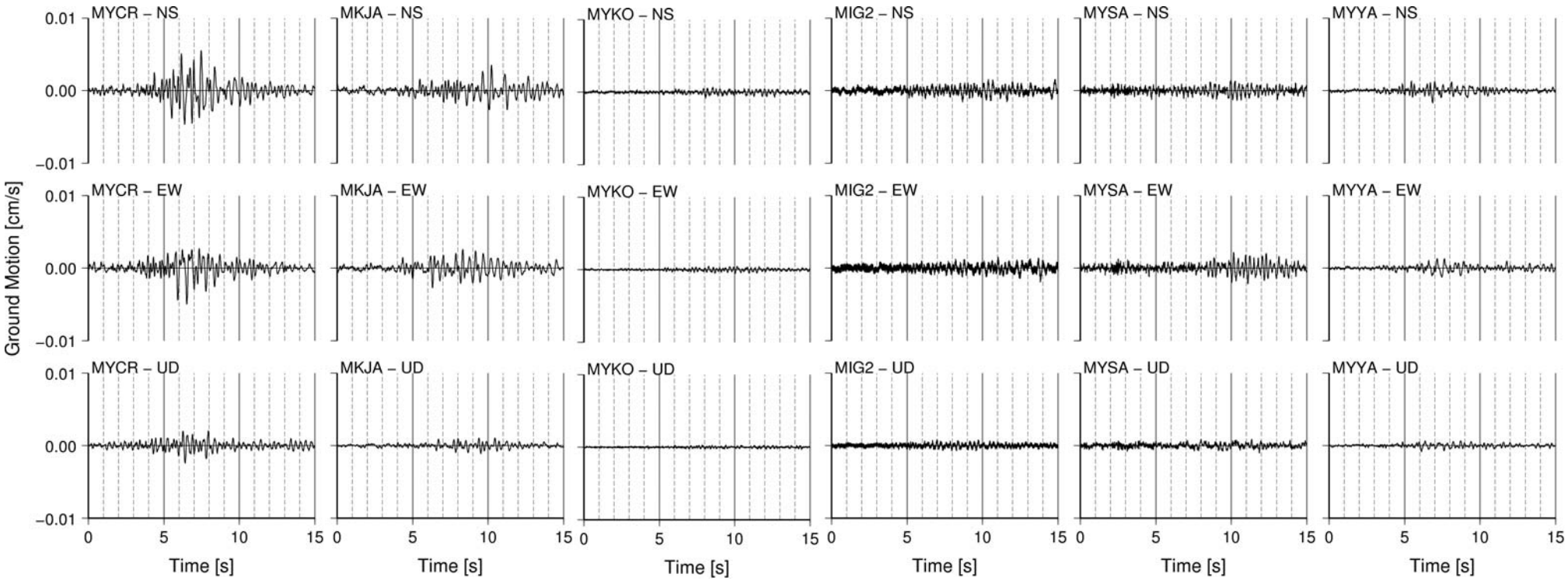

Figure 13. All the seismograms from Miyake Island for quake A' in Figure 11 (a). The origin of the abscissa axis in each panel is the same (18:44:57). MYCR is located at the mountaintop. MKJA is located at the foot of the mountain.

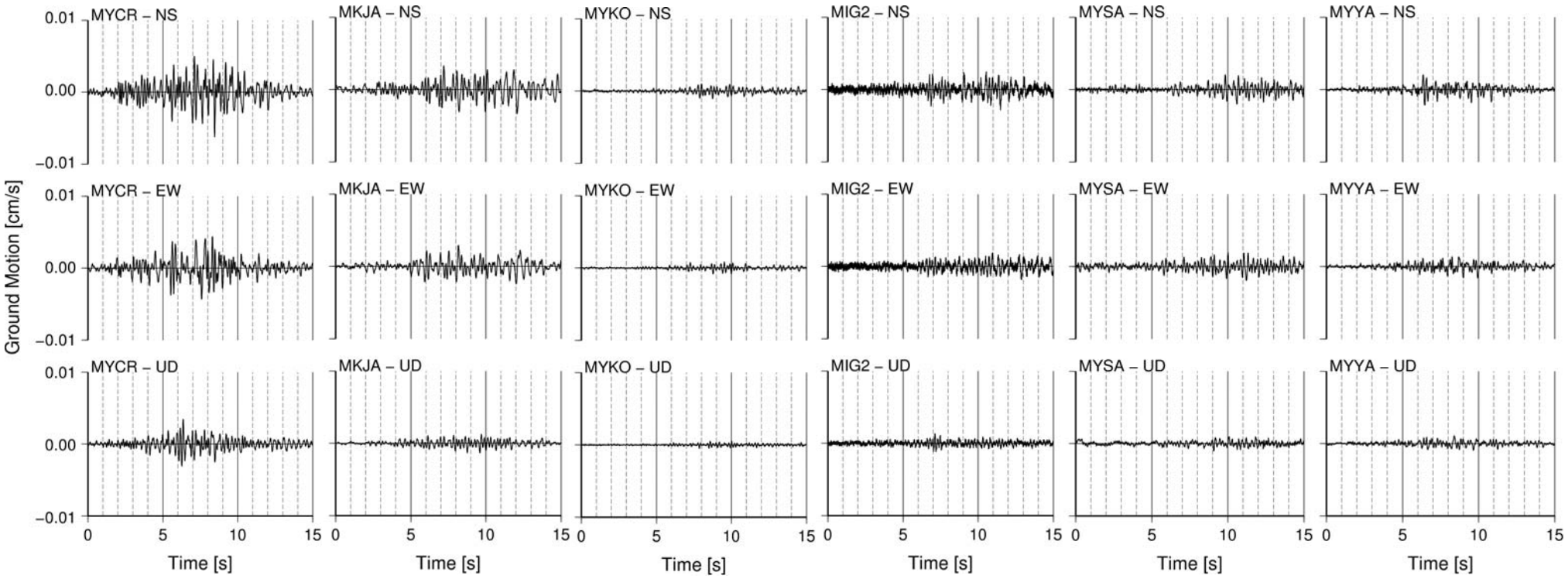

Figure 14. All the seismograms from Miyake Island for quake B' in Figure 11 (a). The origin of the abscissa axis in each panel is the same (20:20:28). MYCR is located at the mountaintop. MKJA is located at the foot of the mountain.

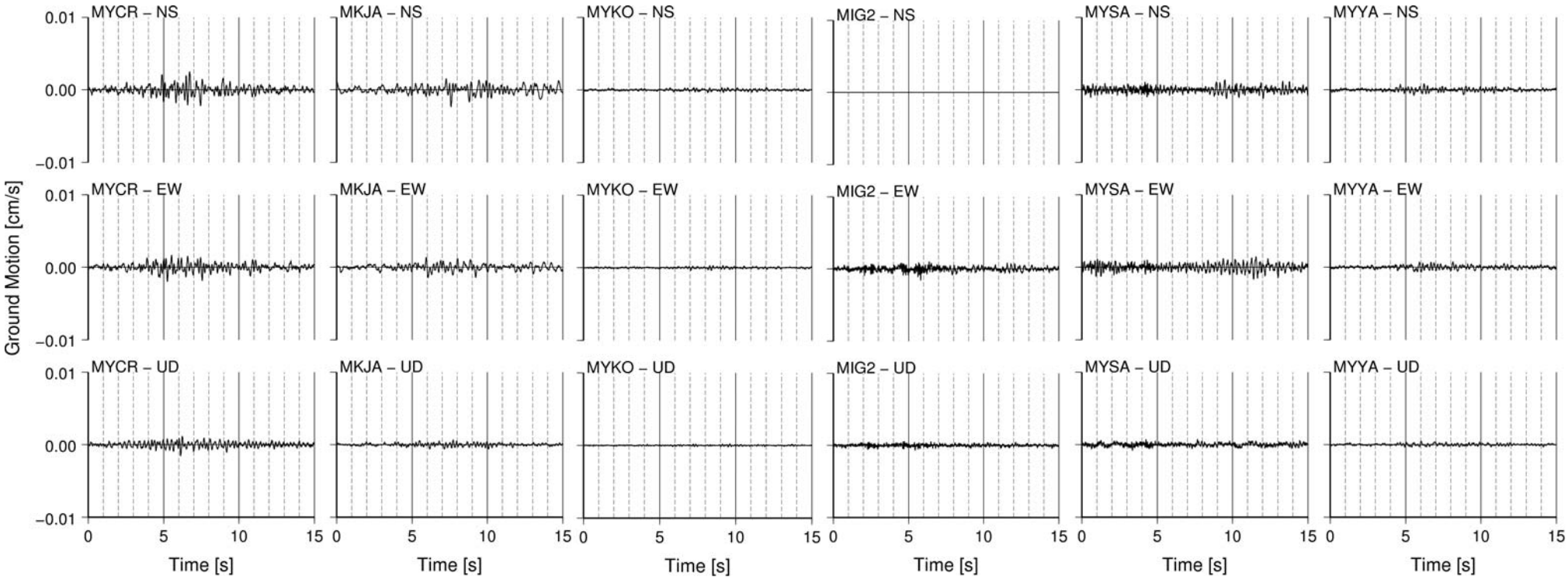

Figure 15. All the seismograms from Miyake Island for quake C' in Figure 11 (a). The origin of the abscissa axis in each panel is the same (21:45:24). MYCR is located at the mountaintop. MKJA is located at the foot of the mountain.

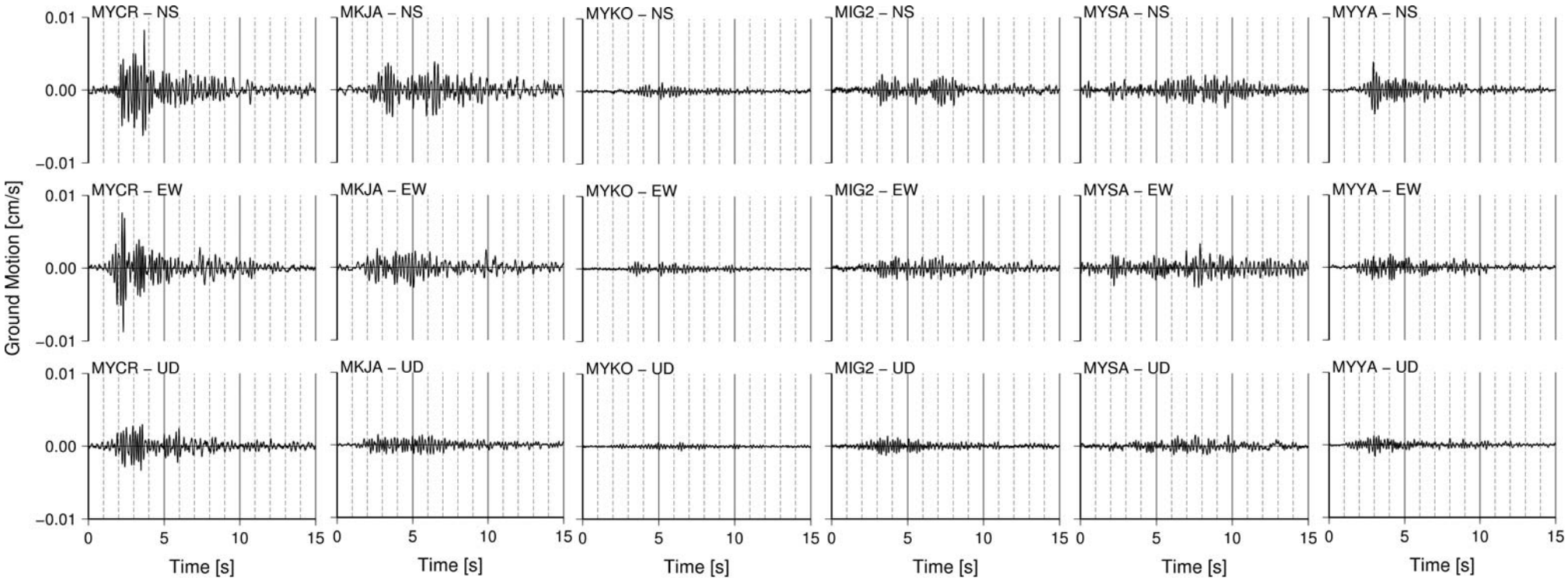

Figure 16. All the seismograms in Miyake Island for quake D' in Figure 11 (a). The origin of the abscissa axis in each panel is the same (00:25:42). MYCR is located at the mountaintop. MKJA is located at the foot of the mountain.

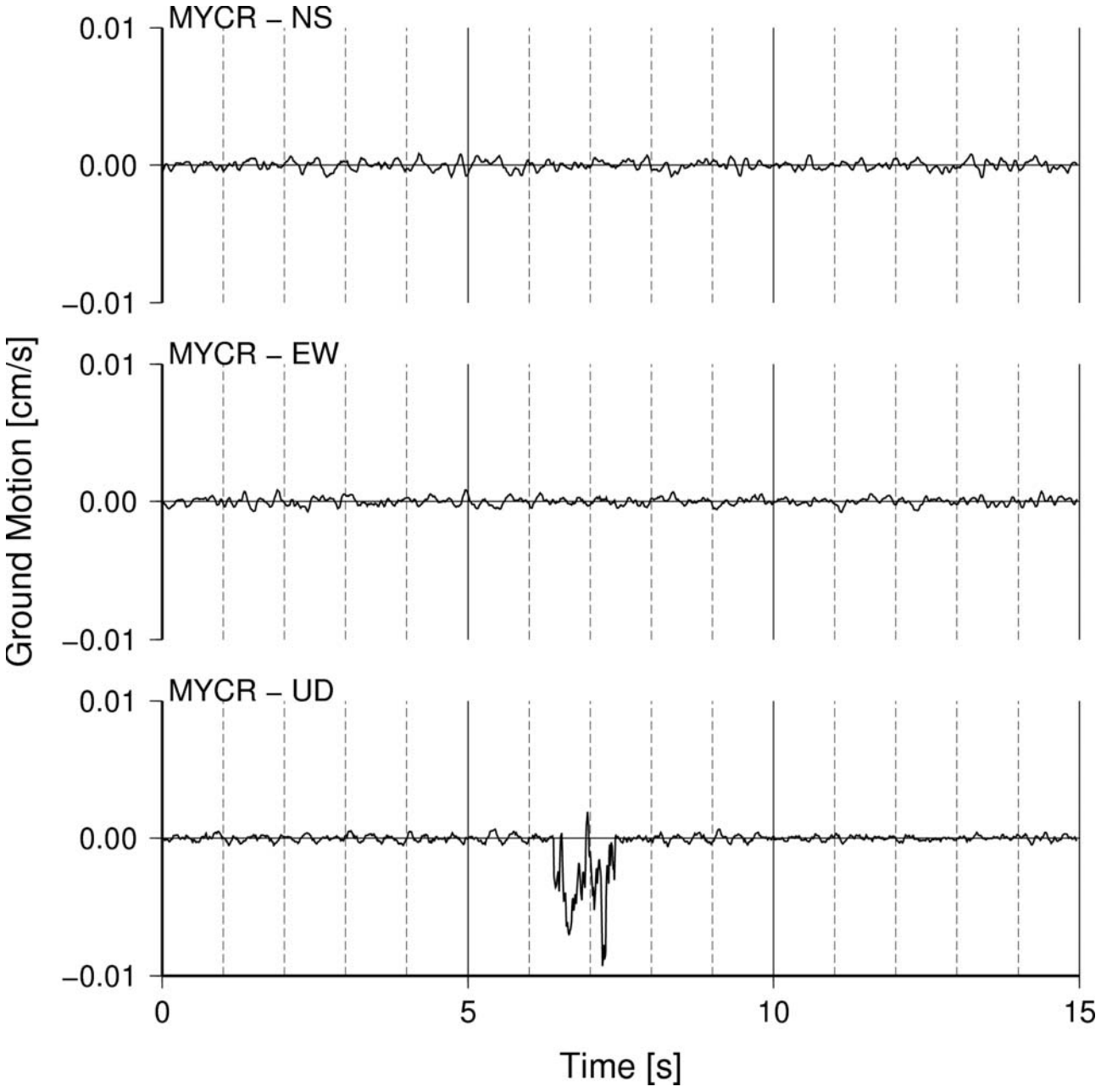

Figure 17. Seismogram of MYCR at E' in Figure 12 (a). The origin of the abscissa axis in each panel is the same (04:43:28).

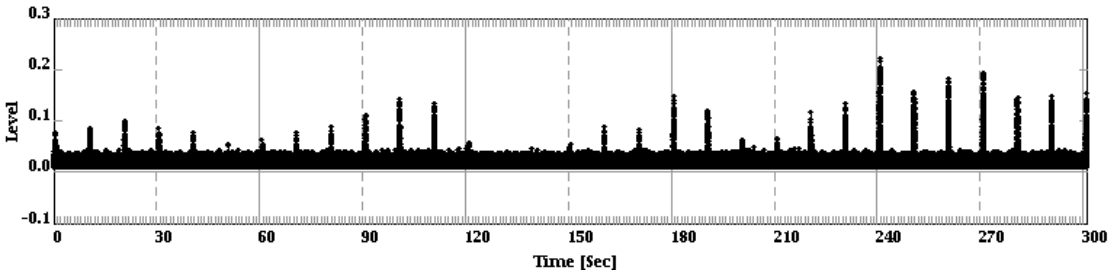

(a) Periodic signal with 10-second intervals.

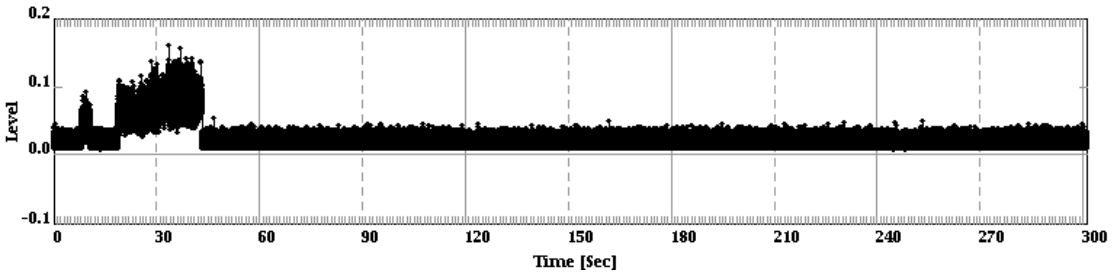

(b) High frequency with abrupt appearance and the noise level offset.

Figure 18. Two kinds of artificial interference removed from the microwave data received at the mountaintop and the mountain foot.

Table 1. Estimation of S/N ratios of microwave signals due to rock fractures. In laboratory: Sample volume = 3.4×10^{-5} m^3, quartzite. In field test: Distance between a rock fracture and the receiver = 2×10^3 m, Noise figure = 3 = 5 dB.

Term	300 MHz	2 GHz	22 GHz
Wavelength [m]	1	0.15	0.0136
Bandwidth [Hz]	3×10^7	2×10^8	5×10^8
Emitted power in the experiment [W]	5.6×10^{-12}	2.7×10^{-11}	1.73×10^{-12}
Radius of crashed rock sphere [m]	10	10	10
Volume of crashed rock sphere [m^3]	4.2×10^3	4.2×10^3	4.2×10^3
Extrapolated microwave emission [W]	6.9×10^{-4}	3.3×10^{-3}	2.1×10^{-4}
Propagation loss of the ground	1	1	1
Antenna gain	10 dBi = 10	15 dBi = 31.6	15 dBi = 31.6
Received signal power [W]	1.09×10^{-11}	3.8×10^{-12}	1.92×10^{-15}
Noise power [W]	3.5×10^{-13}	2.3×10^{-12}	5.8×10^{-12}
Signal to noise power ratio	31	1.7	3.3×10^{-4}

Table 2. Eight periods when lightning strike data were investigated.

Periods
0:00:00 – 23:59:59, Jan. 09, 2008
0:00:00 – 23:59:59, Jan. 12, 2008
0:00:00 – 23:59:59, Jan. 18, 2008
0:00:00 – 23:59:59, Jan. 21, 2008
0:00:00 – 23:59:59, Jan. 23, 2008
0:00:00 – 23:59:59, Feb. 02, 2008
0:00:00 – 23:59:59, Feb. 03, 2008
0:00:00 – 23:59:59, Feb. 04, 2008